Three-Dimensional RF Sensor Networks for Widespread Spectrum Monitoring

Nikolaus Kleber^o, Member, IEEE, Jonathan D. Chisum, Senior Member, IEEE, Bertrand Hochwald^o, Fellow, IEEE, and J. Nicholas Laneman, Fellow, IEEE

Abstract—Spectrum monitoring could improve spectral management and efTiciency by enabling spectrum sharing, strengthening policy enforcement, and facilitating data-driven modeling of RF environments. This paper considers spectrum monitoring sensor networks in three dimensions to extend previous work on two-dimensional models. We derive a closedform expression for the probability of emitter detection, which acts as a metric for system design. We find optimal antenna half-power beamwidths for emitter detection. Additionally, we find that for a path loss exponent less than approximately 3.22, directional antennas are optimal. Otherwise, omnidirectional antennas are optimal. Further, despite potential sub-optimality, omnidirectional antennas are found to be robust in changing environments. Finally, a survey of antenna gain models is evaluated against real antennas to validate the choice of gain model in the paper.

Index Terms—Directive antennas, radio spectrum management, cooperative spectrum sensing.

I. INTRODUCTION

PECTRUM monitoring (SM) is a collection of sensors that measure RF activity over frequency, time, and space [1]. The measurements could provide the "ground truth" of spectrum usage rather than relying solely on theoretical models of limited accuracy or unverified claims of usage by incumbents of spectral rights. Therefore, SM could close the feedback loop for spectrum management by providing spectral observations to guide policies and later to see the effects.

If widespread, SM could enable several applications. SM could inform secondary users in dynamic spectrum access (e.g., by acting as the environmental sensing capability (ESC) [2], [3] for a spectrum access system (SAS) [4], [5]). SM could also help automate spectral policy enforcement by

Manuscript received March 24, 2021; revised August 7, 2021 and November 3, 2021; accepted December 27, 2021. Date of publication January 6, 2022; date of current version June 9, 2022. This work was supported in part by the U.S. National Science Foundation (NSF) under grants 1439682, 1117365, and 2132700, by Intel and the NSF under grant ECCS-2002921, and by the Army Research Laboratory (ARL) under grant W91 INF-16-2-0140. The associate editor coordinating the review of this arti_cle and approving it for publication was Y. Zeng. (Corresponding author: Nikolaus Kleber.)

Nikolaus Kleber was with the Department of Electrical Engineering, University of Notre Dame, Notre Dame, IN 46556 USA. He is now with the EWS Department, RIS, Raytheon Technologies, Fort Wayne, IN 46808 USA

finding "bad actors," capturing evidence, and locating the culprit emitters [6], [7]. Further, SM could provide big data ("Big RE') for data-driven modeling of RF environments and spectrum usage A thorough discussion of these and other potential SM applications can be found in [1 1, Ch. II. Overall, SM could improve spectral efficiency by enabling better spectrum management, enforcement of rules, and improved applications for secondary use.

In our previous work [12], we addressed a missing component of emitter directivity in wireless sensor networks by creating a general framework for both directional emitters and sensors to analyze SM system design. In particular, we focused on a two-dimensional (2D) deployment design. The 2D model provided substantial insights for design choices within a SM system, such as the explicit relationship between emitter detection probability and average sensor density, a measurable trade-off between sensor quality and quantity, and the optimal azimuth antenna beamwidth, to name a few.

The framework extends to three dimensions (3D), which is beneficial to address some short-comings of the 2D model. In particular, the 2D model does not gracefully account for the elevation portion of the antenna pattern. The model shows that the optimal elevation beamwidth approaches zero, which is not realistic. The conclusion is to have the elevation beamwidth as narrow as practical, but no specific value is given. The 3D model in this paper, on the other hand, eliminates such vagueness and provides an optimal value for elevation beamwidth. A closely related issue is that the 2D model limits the emitter and sensor locations to be coplanar. The 3D model allows for more realistic deployment scenarios in which emitters and sensors can operate at varying heights. Similarly, the 2D model limits rotation to be solely azimuthal. The 3D model, in contrast, realistically captures all possible antenna orientations, which are likely to occur in the crowdsourcing scenario motivating the deployment model. Finally, because the 3D model accounts for the full antenna pattern, we are able to consider more antenna gain models and evaluate which is most accurate for our metric of interest, for both the 2D and 3D cases.

A. Contributions

This paper extends the results of [12] to more realistic 3D scenarios. In particular, we investigate the effects of emitter directivity on SM system design and find the average sensor

2332-7731 @ 2022 IEEE. Personal use is permitted, but republication/redistribution requires IEEE permission. See https://www.ieee.org/publications/rights/index.html for more information.

(e-mail: nikkleber@gmail.com).

Jonathan D. Chisum, Bertrand Hochwald, and J. Nicholas Laneman are with the Department of Electrical Engineering, University of Notre Dame, Notre Dame, IN 46556 USA (e-mail: jchisum@nd.edu; bhochwald@nd.edu; inl@nd.edu).

Digital Object Identifier 10.1109nccN.2022.3140770

density to achieve a given confidence of detection. Moreover, we find optimal antenna beamwidths for sensor design in a SM system, which is a function of the environmental path loss exponent, a. We show that if a < 3.22, directional antennas

optimize the probability of emitter detection. Otherwise, omnidirectional antennas are optimal. We further quantify the difference between optimal and sub-optimal designs, demonstrating that omnidirectional antennas are a robust design choice for environments with varying a. Additionally, this paper presents a survey of potential antenna gain models for the framework in [121 and simulates their accuracy against real antennas. The results verify the selection of the gain models used in this paper and in [12].

B. Related Works

The survey in [13] reviews the significant differences between 2D and 3D wireless sensor networks (WSNs) with a focus on network protocols, connectivity, and localization in 3D WSNs. The motivating 3D examples are aerial and underwater WSNs. The survey only mentions the difficultly of multi-path fading and recommends directional antennas as a topic for future research. Similarly, the work in [14] considers 3D non-cooperative spectrum sensing in secondary networks for air traffic control, but only considers a simple distancebased path loss model. In contrast, this paper moves in the recommended direction with an RF model including fading, shadowing, and antenna directivity.

Several works consider the placement and orientation of directional sensors on a 3D terrain [15]. Many jointly optimize multiple objectives, such as maximum coverage, connectivity uniformity, and minimum deployment cost [16]-[18]. These approaches have even been considered for indoor use with constraints particular to the building [19]. In contrast, our work is motivated by crowdsourcing low-cost sensors (e.g., [20]), which results in random sensor locations and orientations. While not constrained to a terrain, [21] considers 3D directional sensors also with a focus on algorithmic optimization of orientations to maximize coverage. The aforementioned optimization problems are solved through complex search algorithms, which are time-consuming and must be repeated for any change in system parameters. Our result provides a closedform expression for quick analysis over all system parameters to provide design insights. Our work also physically links directivity (angle-of-view) to gain (sensing range) to optimize antenna design.

Other works share similar 3D models but differ in focus or scope. Jung and Lee consider directional transmission for secrecy within WSNs of different spatial distributions [22], [23]. Our work shares the random spatial distributions of directional nodes but focuses on emitter detection. Some works share similar RF models within 3D WSNs, but their focus is on emitter localization via measured power and additional measurements, such as time of arrival (TOA) or angle of arrival (AOA) [24], [25]. Motivated by a low-cost sensor, our work considers received power with the simpler goal of detection, whereas TOA and AOA require more complex sensors with time-synchronization and antenna arrays, respectively. Wei et al. consider an unmanned aerial vehicle (UAV) network modeled as a homogeneous Poison point

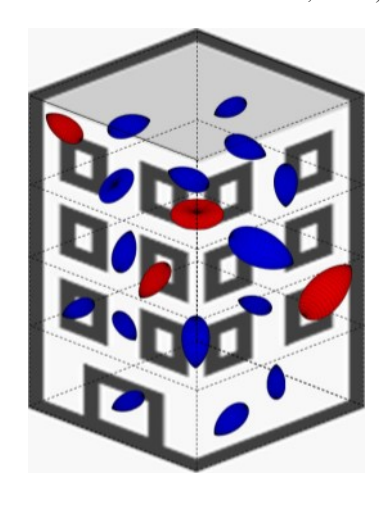


Fig. 1. Illustration of a widespread spectrum monitoring system in three dimensions. Sensor and emitter gain patterns are shown in blue and red, respectively.

process (PPP) with the motivation of providing service coverage in disaster management [261. Their channel model includes path loss, fading, and directional antennas. Consequently, their work shares many elements of this paper's model. However, their model differs by including an additional 2D PPP for a ground network for end-users. Their focus is the UAV network design, particularly the operating height to optimize transmission capacity via spectrum sharing with the ground network. Additionally, [26] models a particular reference antenna and fixes its orientation on the UAVs parallel to the ground, In contrast, this paper considers random orientations and generalizes the antenna model to trade-off angle-of-view and sensing range.

C. Outline

The remainder of this paper is organized as follows. Section II presents the 3D framework to model a SM system and states the problem of interest. Section III provides the general result for the probability of a SM system to detect a single emitter and analyzes the result for optimal designs. Section IV evaluates various gain models against real antennas and verifies the model used in this paper. Section V considers system operation over multiple frequency bands. Section VI gives a lower bound for multi-emitter detection probability and also an expression for the expected number of undetected emitters. Finally, Section VII summarizes our concluding remarks and directions for future work.

II. SYSTEM MODEL

The generalized model used in this paper is described in detail in our previous work [12]. We focus on the 3D version here. We briefly restate the main model components and expound on differences from [12] for three dimensions.

The scenarios of interest include crowdsourced sensors in the commercial context (e.g., cell-phones as sensors). The sensor deployment is well-modeled as uniformly random. As illustrated in Fig. 1, we need to describe locations and orientations via a deployment model, the sensor and emitter

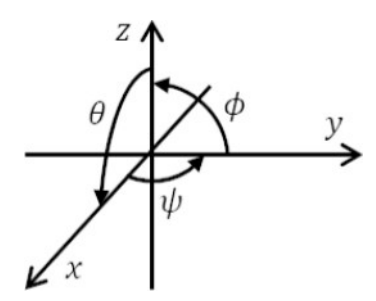


Fig. 2. ne components yaw (V), pitch (0), and roll (4) used to describe the rotation of a rigid body.

capabilities via a hardware model, and the RF propagation via a channel model.

Because emitters and sensors share many common parameters, this paper uses the superscript s or e to denote the parameter for a sensor or emitter, respectively. If there are n^s sensors and n e emitters, the subscripts $j \in \{1, ..., n^S\}$ and $\{1, ..., n^e\}$ denote the index of the sensor and emitter, respectively. For example, a generic location will be denoted by x, the jth sensor location by x^s ., and the jth emitter location by j0.

A. Deployment Model

We consider scenarios in which we have no prior knowledge of sensor or emitter locations nor their orientations. In this case, the sensor and emitter deployment is well modeled as random in location and orientation with the most uninformative distribution.

- I) Locations: We denote location with a vector $x \in R^3$ in Cartesian coordinates. We consider a random deployment within a building in which the deployment of sensors in latitude, longitude, and altitude is reasonably modeled as uniformly random. As a result, the locations of the sensors are well-modeled by a homogeneous Poisson point processes (PPP), denoted d) S , with density [27]. Mathematically,
- $s = (xj) j \in \mathbb{N}$. This model could also apply to aerial networks [13]. Note that conditioning the number of locations in a finite region R C IR³ results in iid uniform locations in R, forming a binomial point process (BPP) [27].
- 2) Orientations: We define the orientation of an antenna as a rotation from a default orientation. Conventionally, the default orientation is such that the antenna's main lobe lies on a coordinate system axis. In three dimensions, a rotation can be realized in multiple ways, including a uniformly random rotation matrix, a normalized vector of four independent standard Gaussian random variables (a quaternion representation), or appropriate probability distributions for the angles of yaw, pitch, and roll. Physically, it is intuitive to use the convention of yaw (V), pitch (9), and roll (+) shown in Fig. 2, which also corresponds to Givens rotations. In particular, we denote rotation with an orthogonal matrix R, which is a product

of Givens rotations. Consistent with matrix multiplication, the order of these rotations matters.

To rotate a rigid body G C IR³, we multiply by the orthonormal Givens rotations,

$$(\psi) = \begin{bmatrix} \cos \psi & -\sin \psi & 0\\ \sin \psi & \cos \psi & 0\\ 0 & 0 & 1 \end{bmatrix}$$

$$(\theta) = \begin{bmatrix} \cos \theta & 0 & \sin \theta\\ 0 & 1 & 0\\ -\sin \theta & 0 & \cos \theta \end{bmatrix}$$

$$(\phi) = \begin{bmatrix} 1 & 0 & 0\\ 0 & \cos \phi & -\sin \phi\\ 0 & \sin \phi & \cos \phi \end{bmatrix}.$$

$$(y) = \begin{bmatrix} 1 & 0 & 0\\ 0 & \cos \phi & -\sin \phi\\ 0 & \sin \phi & \cos \phi \end{bmatrix}.$$

The general rotation is simply

$$R(\psi, \theta, \phi) = R_z(\psi)R_y(\theta)R_x(\phi).$$

We rotate the set of points defined by G by rotating all elements in the set. Mathematically, $R(\emptyset, O, \phi)\mathcal{G} = \{R(\emptyset, O, : x \in G\}.$ To simplify notation, when we refer to the rotation of the ith emitter or jth sensor antenna, we will use the notation R^e and R^e , respectively, where we have dropped the input $[\psi^e_i, \theta^e_i, \phi^e_i]$ and $[\psi^s_i, \theta^s_i, \phi^s_i]$.

B. Hardware Model

As in [12], the emitters share a common gain pattern (gf g ^e V i), and the sensors are deployed with the same antennas (g; g ^s V j). This scenario is reasonable because emitters operating in the same frequency range likely have similar antennas, and a widespread deployment would likely use mass-produced sensors with nearly identical antennas. For similar reasons, we say that the sensors have the same sensitivity (Tj^s T ^s j). Finally, we consider scenarios in which all emitter powers are equal and known (p; p ^e Y i) because publicly available regulations usually limit transmission power, and emitters often transmit at the legal maximum to obtain the highest SNR possible.

Finally, we consider scenarios in which discernible differences exist among the emitter signals across time, frequency, spreading codes, and/or high-level protocols. More details can be found in [12].

1) Sensor Sensitivity: Here we define sensor sensitivity and the underlying physical factors that determine its value [28].

Definition 1 [Minimum Detectable Signal (MDS)]: Let T^S denote the power of the minimum detectable signal by the sensor.

We mathematically express MDS (linearly) as $\tau^s \triangleq \nu(\text{SNR}_{\text{out}})k_BBT$,

where v is the device noise figure, SNRout is an application based minimum SNR, kB is the Boltzmann constant, T is the system temperature in Kelvin, and B is the system bandwidth [29]. A full explanation of this expression is in [12, Sec.II-B].

Remark 1: The power of the emitter signal received by the sensor must be greater than T ^S for the sensor to distinguish the emitter signal from noise.

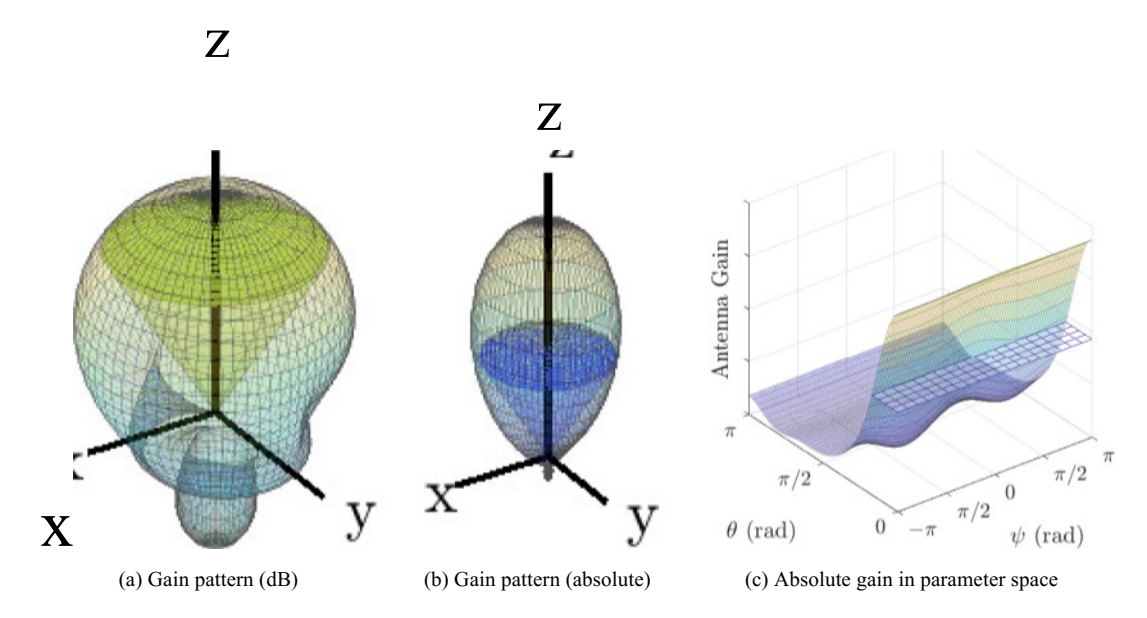


Fig. 3. An example taken from MATLAB's toolbox of an antenna radiation pattern in three dimensions compared to our simplified radiation pattern.

2) Antenna Gain Pattern: This paper uses the general antenna model from [121. In particular, the antenna gain pattern is simplified with the concept of half-power beamwidth (HPBW). The HPBW is the angular range between the points at which the gain has decreased 3 dB from the peak gain [30]. An antenna can be characterized with two HPBWs measured perpendicular to each other. For this work, we consider the azimuthal HPBW, denoted W, and the elevational HPBW, denoted e. The HPBWs and maximum gain of an antenna, denoted go, are physically related [29]. In general, as the HPBWs narrow, go increases. Formally, the maximum gain is a function of the HPBWs: go(W, 9).

We simplify the gain pattern to be constant at go/2 when the direction of departure (DoD), or equivalently direction of arrival (DoA), is within the HPBWs and zero elsewhere. To evaluate the DOD, we require the antenna position (p e IR³), the target location (t e IR³), and the antenna orientation (R e $12^{3 \times 3}$) as inputs to the gain function: g(p, R, t). The normalized DOD is

$$R^{-1} \frac{\mathbf{t} - \mathbf{p}}{\mathbf{l} \cdot \mathbf{l} \cdot \mathbf{r} \cdot \mathbf{p} \cdot \mathbf{l}}$$
.

We offer a high-level mathematical expression to conceptualize the gain simplification:

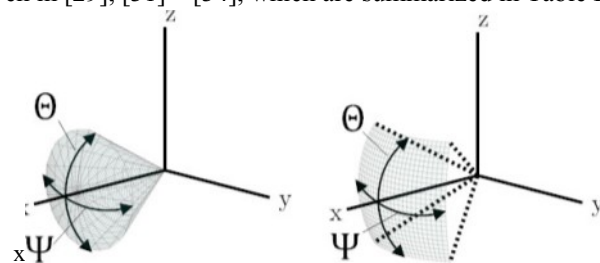
$$g(p, R, t)$$
 — $g_0(\Psi_{,e})$, DoD is within HPBWs (2)

Fig. 3 illustrates the simplification, which captures the essence of directional antennas.

The simplification in (2) can have multiple realizations. In particular, one must consider the geometric shape of the simplified antenna pattern and the functional form of go(W, 9). The simplified shape affects the condition that the DOD is within the HPBWs. Clear choices of shape include the spherical cap and spherical quadrilateral, illustrated in Fig. 4.

Exact expressions for the form of go(W,9) are few in number and are often complex, but some approximations have

developed over the years. We consider the approximations given in [29], [31]—[34], which are summarized in Table I.



(a) Spherical cap (b) Spherical quadrilateral Fig. 4. Illustration

of simplified antenna pattern shapes.

First, we discuss forms of go(W, 9) corresponding to two very general cases. Directional antenna patterns with a single, symmetric lobe are well-modeled with a radiation intensity function

$$U(O, d') cos^m O, O[0, T/2],$$
 [0, 2m), (3)

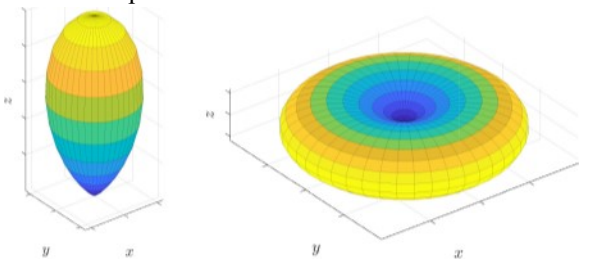
where m 2 0 can be varied for the width of the beam [29]. Similarly, omnidirectional antenna patterns with a single, symmetric lobe are well-modeled with a radiation intensity function

$$U(\theta, \psi) = \sin^{m} O, O \in [0, T],$$
 [0, 2K). (4)

Fig. 5 illustrates these functions. With [29, eq. (2-21)], the closed-form expressions of (3) and (4) provide an exact go(W, 9) given in Table I. Note that we assume antenna efficiencies of 1 without loss of generality. See [11, Appendix A] for the derivation.

The approximation by Kraus in [31] can be motivated from the concept of beam solid angle for antenna patterns with one narrow major lobe [29, Ch. 2]. Tai and Pereira consider the case of broadside arrays of short dipoles and an arithmetic mean of two perpendicular planes of the farzone electric field, though their result can extend well to any directional single lobe

antenna pattern [32]. McDonald creates his approximation for omnidirectional antennas based on broadside collinear arrays with a radiation pattern based on



These two approximations well-model a wide class of antenna patterns despite limitations of symmetry and no side lobes. Furthermore, the approximations provide closed-form expressions that can be analyzed.

C. RF Channel Model

This paper re-uses the channel model in [12], which provides a thorough discussion on the model details. Here we highlight the essential points. The channel incorporates environmental aspects such as large-scale shadowing and smallscale fading to

 $\label{eq:table 1} TABLE~1$ APPROXIMATIONS OF THE MAXIMUM GAIN VALUE go(W , 9)

L	abel	Author	$g_0(\Psi,\Theta)$	Notes
A		Kraus	$\frac{4\pi}{\Psi\Theta}$	directional single lobe
В		Tai & Pereira	$\frac{\frac{4\pi}{\Psi\Theta}}{\frac{32 \ln 2}{\Psi^2 + \Theta^2}}$	directional single lobe
C	:	[29]	$2(m+1), \ m = \frac{\ln(\frac{1}{2})}{\ln\left(\cos\left(\frac{\Theta}{2}\right)\right)}$	directional single, symmetric lobe; derived from (3)
D)	McDonald	$\frac{101\pi/180}{\Theta - 0.486\Theta^2/\pi}$	omnidirectional single lobe
Е		Pozar	$-172.4 + 191\sqrt{0.818 + \pi/(180\Theta)}$	omnidirectional single lobe
F		[29]	$\frac{2\Gamma\left(\frac{m+2}{2}+\frac{1}{2}\right)}{\sqrt{\pi}\Gamma\left(\frac{m+1}{2}+\frac{1}{2}\right)}, \ \ m=\frac{\ln(\frac{1}{2})}{\ln\left(\cos\left(\frac{\Theta}{2}\right)\right)}$	omnidirectional single, symmetric lobe; derived from (4)
(a) cos ⁿ	nО		(b) sire ⁿ O	determine the power received by a sensor from an em

Fig. 5. Illustration of the radiation intensities given by (3) and (4).

the sinc function [33]. Pozar uses curve-fitting on the common omnidirectional radiation pattern in (4) to obtain his result [34].

In Section IV, we compare the various combinations of shapes and forms of , 9) in Table I to verify which is the best model for this paper. For ease of exposition, the remainder of the paper will associate a "directional antenna" with the approximation given by the spherical cap and gain value C from Table I. Likewise, an "omnidirectional antenna" will be approximated by the spherical quadrilateral and gain F for goop, e).

Mathematically, the simplified gain function of a directional antenna is

$$Ydir(p, R, t) - (5) \begin{cases} \frac{\ln(\frac{1}{2})}{\ln(\cos\frac{\Theta}{2})} + 1, & R - 1^{t-P} \in Ddir \\ 0, & else \end{cases}$$

where Ddir is the set given by

Ru { (r, 9) e IR 3 • r 1, q/' e [0, 2K), o [0, 9/2]}. Similarly, the simplified gain function of an omnidirectional antenna is gomni (p, R, t)

$$= \begin{cases} \frac{\Gamma\left(\frac{\ln\left(\frac{1}{2}\right)}{2\ln\left(\cos\frac{\Theta}{2}\right)} + \frac{3}{2}\right)}{\sqrt{\pi}\,\Gamma\left(\frac{\ln\left(\frac{1}{2}\right)}{2\ln\left(\cos\frac{\Theta}{2}\right)} + 1\right)}, & R^{-1}\frac{\mathbf{t}-\mathbf{p}}{\|\mathbf{t}-\mathbf{p}\|} \in \mathcal{D}_{\text{omni}} \\ 0, & \text{else} \end{cases}$$

where
$$\Gamma(z) \triangleq \int_0^\infty t^{z-1} \, \mathrm{e}^{-t} \, \mathrm{d}t$$
 and $\mathcal{D}_{\mathrm{omni}}$ is
$$\left\{ (r, \psi, \theta) \in \mathbb{R}^3 : r = 1, \psi \in [0, 2\pi), \theta \in \left[\frac{\pi - \Theta}{2}, \frac{\pi + \Theta}{2}\right] \right\}.$$

determine the power received by a sensor from an emitter. From a system perspective, the channel can incorporate the emitter and sensor antenna gains. For ease and wide-applicability, we use the approximation given by the simplified path loss model in [35, eq, (228)] and add a fading variable. Let us briefly define some notation. Let pi be the power received by sensor j from emitter i. Let llxt€ — xjll denote the Euclidean distance between the ith emitter and jth sensor. Let a 2 2 be the path loss exponent determining the rate of power attenuation. Let hij be from a family of independent and identically distributed (iid) random variables to account for fading (or the product of fading and shadowing) between the ith emitter and jth sensor. In general, we have pi hog; (x s R s x ex; , Rf,x; K llxt \$11 -a pf,

where K incorporates other aspects of signal attenuation and antenna characteristics. A common form of $K \equiv (c/4Tfm)^2 r'$, where is a reference distance and c is the speed of light [35], [36]. If a 2 and hij 1, this choice of K results in Friis equation for free space.

In practice, the jth sensor computes a time-averaged power within a given bandwidth, which is modeled by

$$p_j^s \triangleq \sum_{i=1}^{n^e} p_{ij}^s + N_0,$$

where No vkB TB is the thermal noise in the receiver. Without a priori knowledge of n $^{\rm e}$, interpretations on p? alone can be complicated if n $^{\rm e}$ > 1. Consequently, we consider scenarios in which the sensors have the capabilities to separate emitter signals and powers via low-level signal processing (see [12, Sec. II-B] for more details). We also note that the receiver chain will introduce additional noise, which is accounted for by the sensor's noise figure v. As a result, we use the sensor MDS T $^{\rm S}$ from (1) when evaluating whether the sensor can distinguish any emitter signal from noise.

D. Problem Statement

This paper focuses on the probability of emitter detection as a key metric to aid the design of a SM system. Let us formally define emitter detection before stating the problem.

Definition 2 (Emitter Detection): The jth sensor detects the ith emitter if pi T S. Further, the sensor network detects the ith emitter if at least one sensor detects the emitter. Let Ei denote the ith emitter's detection by the sensor network. Mathematically,

$$\left\{p_{ij}^{s} \ge \tau_{s}\right\} \tag{8}$$

Remark 2: In the case of a single emitter, we locate the emitter at the origin without loss of generality because the sensor locations form a stationary PPP. To simplify notation for this case, we drop the index and denote the detection event as E. If the emitter locations form an independent stationarity point process, the emitter at the origin is the typical emitter [27].

Ultimately, we want to find Pr(E) as a function of the system parameters and use the expression to find optimal parameter values, particularly for the sensor design. Additionally, we want to see how system parameters affect the sensor density necessary to achieve an arbitrary confidence of emitter detection.

III. RESULTS FOR SINGLE EMITTER

A. General Result

Proposition I: Let be a stationary PPP of intensity λ and (Mx)xe+ a family of iid non-negative random variables (marks), independent of with finite moment $E[Mx^{3/Q}]$. For

$$> 0$$
, the random variable
$$N \triangleq \sum_{\mathbf{x} \in \Phi} \mathbb{1}[M_{\mathbf{x}} || \mathbf{x} ||^{-\alpha} > \gamma]$$

is Poisson with mean

$$EIN] = \lambda \frac{4}{3} \pi \gamma^{-}_{\ddot{o}} E[M^{\ddot{o}}],$$

where M is distributed like all NIX and ö 3/0. In particular,

$$Pr(N > 0)$$
 1-
= 1 —exp(${}^{\circ}E[M^{\circ}]$). (9)

Proof: The proof is analogous to that given in [12], but with \ddot{o} 3/0 and with integration over IR³.

Remark 3: Let Cd be the volume of the unit ball in d dimensions [27, Eq. (2.7)]:

$$\begin{array}{c}
\text{Cd} \\
 r(d/2+1)
\end{array}$$

Particular to this paper, 03 T. To relate this proposition to that in [12], let \ddot{o} d/a and E[N] = \ddot{o} E[M \ddot{o}] for d 2 and 3.

Remark 4: Without loss of generality, E[M] can be normalized to 1 b' setting M' Mx/E[M] and 1/E[M]. Because E[M] E[M] 1, randomness in the channel (due to fading,

shadowing, or randomly oriented directional antennas) never increases detection probability.

In the context of our problem statement, N is the number of sensors that detect the emitter at the origin. Consequently, the probability of emitter detection Pr(E) Pr(N > 0), which is given

B. Applications

Let be the ratio of the gain function's solid angle to a sphere's solid angle (4T steradians). For a spherical cap and quadrilateral, = $\sin^2(9/4)$ and (W /(27T)) $\sin(9/2)$, respectively. Without loss of generality, let K 1 in the equations below (p e can be replaced with t€p e).

1) Baseline (Isotropic Emitter and Sensors, No Fading): Isotropy means the gain equals I in all directions. Consequently, is the ratio ,/p °. With no fading, M 1. The result is

Pr(E) 1 —
$$\exp(-\lambda^s c_3(p^e/\tau^s)^{\delta})$$
.

2) Non-Isotropic Emitter, No Fading: The emitter transmits in the solid angle fraction ff. The result is an independent thinning of the PPP by Additionally, there is a power gain of g ^e. Therefore,

$$\Pr(\mathbf{E}) = \mathbf{I} - \exp\left(-\lambda^s \eta^e c_3 (g^e p^e / \tau^s)^{\delta}\right).$$

3) Non-isotropic Sensors, No Fading: In this case, the sensor antenna receives in the solid angle fraction The directionality can be taken to be the fading distribution. In this case, the marks NIX are Bernoulli random variables with mean Therefore, E[M ^o] There is also a power gain of g ^s. Thus,

$$\Pr(E) \ 1 - \exp\left(-\lambda^s \eta^s c_3 (g^s p^e / \tau^s)^{\delta}\right).$$

Note that the effect of sensor directionality has the same form as emitter directionality.

4) Non-Isotropic Emitter and Sensors, No Fading: We combine the previous two results to obtain

$$Pr(E) = I - exp^{-\lambda^s \eta^e \eta^s c_3 (g^e g^s p^e / \tau^s)^{\delta}}.$$

5) Non-Isotropic Emitter With Fading: In this case, the iid marks Mx represent fading. The effect is independent thinning of the PPP by the ö-th moment of M. If Rayleigh fading IS present, where Mx are iid exponential with mean 1, then

$$E[M^{\ddot{o}}] = + 5$$
). Thus,

Pr(E) 1 — exp
$$C3F(1 - f-\delta)(g^e p^e)$$

Remark 5: The fading term can be considered a power gain $\Gamma(1+\ddot{o})^{1/\ddot{o}}$, which has a lower bound given by 1/2+(5/2). To (over-)compensate for the fading loss, the emitter gain can be increased by $2/(1 + \ddot{o})$.

Remark 6: If both shadowing and fading are present, M_x can be the product of both random variables.

6) Non-Isotropic Emitter and Sensors With Fading: Here the marks combine the effects of both fading and sensor directionality. Let bx denote the Bernoulli random variables for directional sensors and hx denote the iid fading random variables. Thus, Mx bxhx and $E[M^{\bullet}]$ rt $E[h^{\bullet}]$. The result is

$$\Pr(\mathsf{E}) \ 1 - \exp\left(-\lambda^s \eta^e \eta^s c_3 \mathbb{E}[h^{\delta}] (g^e g^s p^e / \tau^s)^{\delta}\right). \ (11)$$

We note that Pr(E) only depends on the ratio $w \triangleq g^e g^S np\%/T^S$. Therefore, (11) can be compactly written as $Pr(E) = 1 - \exp(-\lambda^s \eta^e \eta^s c_3 \mathbb{E}[h^\delta]\omega^\delta)$.

To find the average sensor density required for an arbitrary confidence of detection, p, we substitute for Pr(E) and solve for AS:

$$\ln(1/(1-(\text{nerd}^{c_3}\mathbb{E}[h^{\delta}]\omega^{\delta}).$$
 (12)

7) Unknown Emitter Gain: As noted in [12], the emitter gain may not always be known. However, Prop. I only requires the statistics of the emitter gain to be known. In particular, let Mx bxhxg $^{\rm e}$, where g $^{\rm e}$ is now a random variable. The variables bx and hx account for sensor directionality and fading, as described previously. We find E[M $^{\rm e}$] bhg $^{\rm e}$) $^{\rm e}$] = $(hg^e)^{\rm o}$], which is substituted

into (9) for $\mathbb{E}[(hg^e)^\delta] = \mathbb{E}[h^\delta]\mathbb{E}[(g^e)^\delta]$, and we have $\Pr(E)$. If h and $\gcd(C)$ are independent, $\exp\left(-\lambda^s\eta^sc_3\mathbb{E}[h^\delta]\mathbb{E}[(g^e)^\delta](g^sp^e/\tau^s)^\delta\right)$.

Recall from Remark 4 that the additional randomness from an unknown emitter gain never increases Pr(E). Finally, note that for (13) to apply in Section VI for multiple emitters, we additionally require that the g/ are iid.

C. Other Point Processes

The PPP exhibits complete spatial randomness [27, Sec. 3.1]. Other point processes can exhibit attraction, resulting in clusters. In the other direction, point processes can exhibit repulsion between points, resulting in a more regular pattern. Consequently, the PPP is an interesting cross-over point that can act as a bound for other point processes.

1) Clustered Point Processes: Given the manner in which people naturally tend to congregate, crowdsourcing the sensor deployment could result in clustering. A sensor network whose sensor locations form a cluster point process will have a detection probability no better than that of a PPP. Intuitively, overlap among sensor coverage regions increases as clustering increases, and the detection probability consequently decreases. In the other direction, as clustering decreases for, e.g., a Neyman-Scott cluster process whose clusters are translated to a parent PPP [27, Def. 3.4], the point process approaches a PPP. Therefore, the performance of the PPP is an upper bound on the performance of a cluster point process. Since the expression for detection probability of a cluster process would be unwieldy, the bound provided by the PPP is a useful result.

In a practical crowdsourcing scenario, not all sensors will participate simultaneously. Under certain circumstances, an independent thinning of a cluster point process will be close to a PPP [37, Sec. 3]. Hence, the PPP model is still reasonable for a crowdsourced sensor deployment.

2) More Regular Point Processes: More regular point processes, such as soft-core and hard-core processes, could resemble sensors spaced between floors within a building or even spaced between separate buildings. Such point processes have a higher detection probability than the PPP for the same density. Intuitively, since the points of a regular point process repel from each other, the sensor coverage regions overlap less. In particular, for isotropic antennas with no fading, the facecentered cubic (FCC) lattice (or the hexagonal close packing lattice) performs the best and bounds the performance of any other point process [38]. For this lattice, let the spacing between sensors be a. The density is = $y/\ddot{a}/a^3$. In the case of no fading with an isotropic emitter and sensors, the sensing range is p = from (7). If a > 2p, the detection probability is at most $c \cdot gp^3$ and if a the detection probability can reach I. Since 2.1 — e $\bar{}$ æ, the performance of the FCC lattice indeed exceeds that of the PPP. The FCC's detection probability in more general cases is explored in Appendix C.

If it is possible to design the spatial deployment of the sensors, the FCC lattice is the obvious choice. In practice, the deployment of sensors would inevitably vary from a targeted distribution. If the points of a lattice are randomly perturbed, the result approaches a PPP if points are displaced a large enough distance [39, Sec. II.C]. Thus, the PPP result is still quite relevant even if the sensor deployment can be designed.

3) Inhomogeneous PPP: For PPPs, the density could be location dependent, denoted (x). For instance, the density could vary with altitude. For inhomogeneous densities, Prop. I would need the following modifications.

Let $\{x e : Mx > IllxII^Q\}$ be the independently thinned version of from Prop. I. Define g(x) as the probability of retaining the point from in at location x. In this case, g(x) EM [1[Mx > IllxIl&]] FM(711xIl^O), where FM is the complementary cumulative distribution function of M. If is an inhomogeneous PPP with density N remains a Poisson random variable, but now with mean

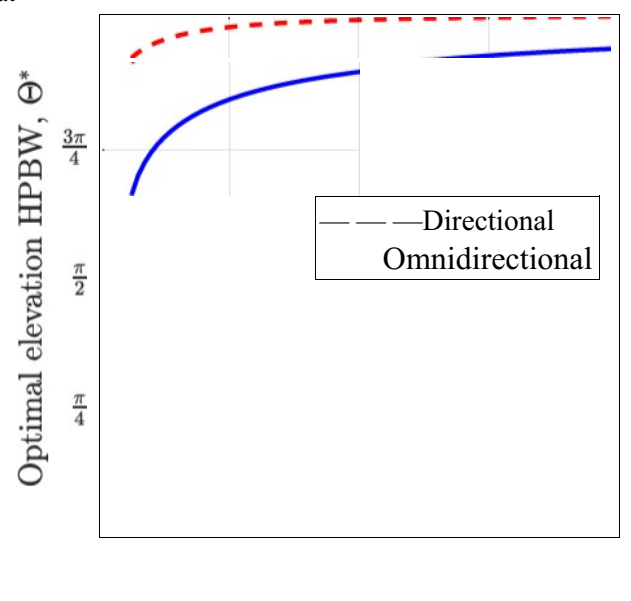
EIN] Mt) d
$$tf(x)g(x) dx$$
,

where f(x) is a spatial probability distribution related to $\lambda(x)$. In particular, if we condition to have n points in a finite region R (resulting in a binomial point process), those n points are distributed in R according to f(x). The proof for (14) is found by substituting an inhomogeneous density within the proof given in [27, Sec. 2.7.3].

Since N is Poisson, we still have Pr(N > 0) 1 _exp(—E[N]) as in Prop. 1, but with no further simplification. The result will be particular to the forms of $\mathcal{N}(x)$, f(x), and FM and will likely require numeric computation.

D. Optimal HPBWs

The antenna design of the sensor can be optimized for detection probability. For either emitter or sensor antenna, note that



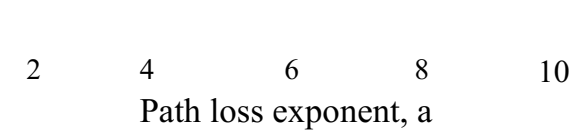


Fig. 6. The optimal elevation HPBW e* for the probability of emitter detection Pr(E) as a function of path loss exponent a. The optimal Θ applies to both emitters and sensors (i.e., = e*).

argmaxPr(E) argmax og .

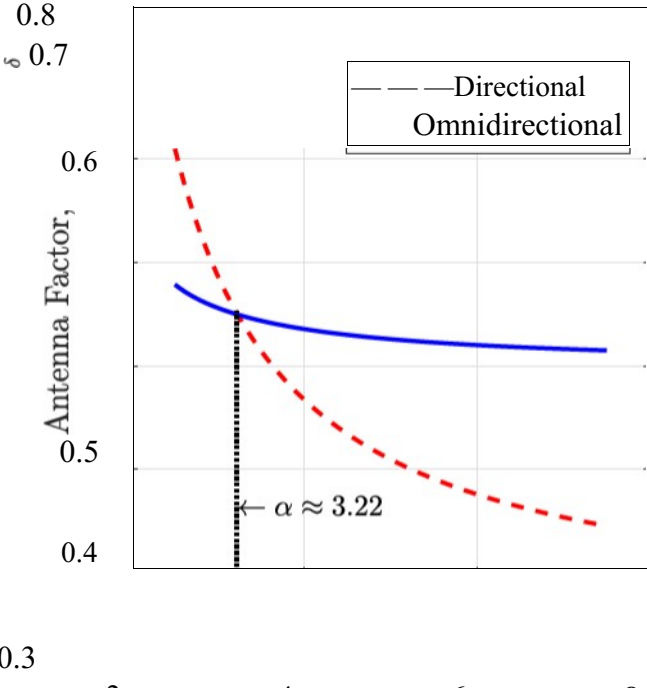
We find the solution by taking the respective partial derivative and setting the result to zero: O and ηg^{-}

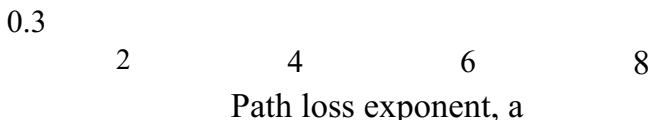
O. For an omnidirectional antenna, 2n by definition (and by inspection of for spherical quadrilaterals). For a directional antenna, by symmetry of the spherical cap, so We use a numeric root solver to find the zeros of and numerically confirm that the solution is a maximum.

See Appendix A for expressions of the derivatives of directional and omnidirectional antennas. Since 9* depends on a, Fig. 6 plots 9* versus a. We offer some observations. First, the optimal HPBW 9* monotonically increases with a. Therefore, in the limit as a 00, 9* approaches its maximum value of T. Qualitatively, as the propagation environment worsens, the optimal antenna becomes more isotropic.

With the optimal HPBWs, we compare the optimal (E) to determine in which scenarios we should use directional or omnidirectional antennas for the sensors. If all other system parameters are equal, comparing the optimal antenna factor η^* (g* between directional and omnidirectional antennas suffices. Here and g* are evaluated with and 9*. See Fig. 7.

Directional sensors have a higher (E) for low values of a, while omnidirectional sensors have a higher (E) for higher values of a. In particular, the two lines intersect at a 3.22, which





can be found numerically from the expression Odir(gdir) omm (g*omm.)^{δ}. In other words, if a < 3.22, directional sensors with optimal 1--1PBWs given by Fig. 6 result in a higher Pr(E) than omnidirectional sensors. On the other hand, a higher probability of detection is achieved using omnidirectional sensors if a > 3.22.

Fig. 7. The antenna factor as a function of path loss exponent a for both directional and omnidirectional antennas with optimal HPBW e* from Fig. 6.

The intuition for this conclusion is in the trade-off between the sensor's angle-of-view and sensing range, which are inherently linked to the antenna directivity and gain, respectively. In general, if the sensor's angle-of-view decreases, the range increases. However, the increase in range is influenced by the path loss exponent a. Let us consider the extreme cases. If the path loss exponent is very high (a + 00), any increase in gain is quickly lost to path loss attenuation, and the resulting increase in range is marginal. Consequently, the sensor covers a larger area by having a wider angle-of-view. On the other extreme, for very low a, any increase in range is undeterred by the path loss attenuation. Consequently, it is worthwhile to trade-off angle-of-view to obtain a larger range. Between these extremes, the trade-off is equivalent at a 3.22.

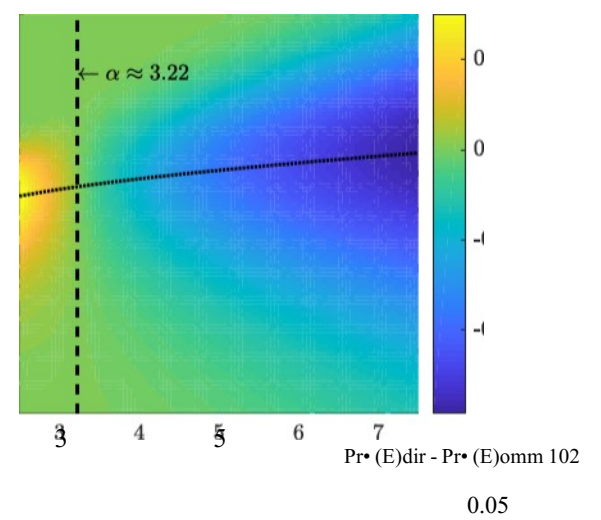
The degree to which directional antennas improve Pr(E) if a < 3.22 depends on the other system parameters. Let C = and D — (g%Ep $^{\rm e}$ /T $^{\rm S}$). Consider the case of Rayleigh fading for which h is exponential with mean 1 and E[hö] = +6). Under these conditions,

Pr(E) 1

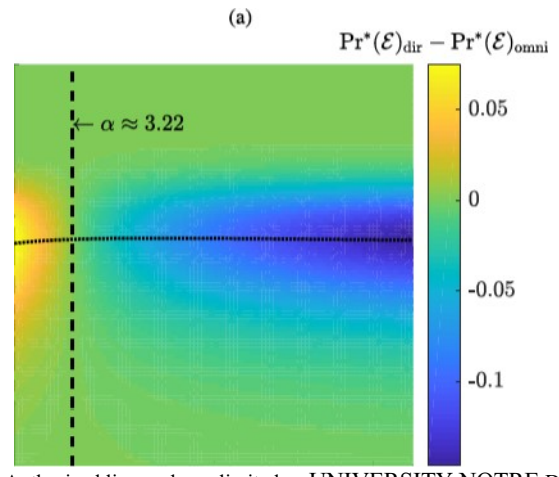
Fig. 8 plots the difference . as a function of D and a (with C 1) and as a function of C and a (with D 1). The dotted line gives the value of D or C, respectively, at which $|Pr^*(\mathcal{E})_{dir}$ — Pr^* (E) . I is largest for a given a. See Appendix B for details.

We observe that at particular values of D and C, a directional antenna can improve $Pr^*(E)$ by about 7.5%. However, other choices of D and C result in negligible improvement in $Pr^*(E)$. Therefore, while directional antennas are mathematically optimal if a < 3.22, in practice omnidirectional antennas could perform nearly as well depending on D and

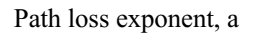
C. From a design perspective, if D and C are such that

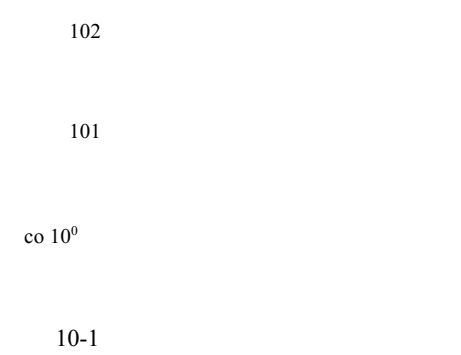






Authorized licensed use limited to: UNIVERSITY NOTRE DAME. Downloaded on July 13,2022 at 18:49:24 UTC from IEEE Xplore_ Restrictions apply





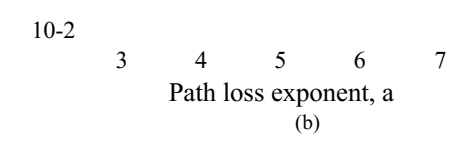


Fig. 8. The difference Pr* (E)dir — omm• (a) as a function of path loss exponent a and system constant D, and (b) as a function of a and system constant C.

 $P_T^*(E)$ dir - (E)omm. is low for a < 3.22, an omnidirectional antenna could be a more robust design as it is optimal for a 3.22 and only marginally suboptimal if a S 3.22. This suggests the use of omnidirectional antennas for scenarios in which a is expected to vary.

IV. MODEL VERIFICATION FOR SINGLE EMITTER

With several approaches to approximate the gain function, we want to validate the model used in this paper, which includes both a shape and value approximation. To evaluate the different approaches, we use Pr(E) because it is the key metric in this work and depends on both the gain value and shape. Because we want the approximations that are most accurate, we compare the gain approximations to representative real antennas. In particular, we use the finite length dipole as our comparison for omnidirectional antennas. Similarly, for directional antennas, we use the representative patch antenna and horn antenna as our benchmarks.

Our approach to determine Pr(E) via simulation follows. First, we simulate random deployments of sensors and the emitter. The emitter is located at the origin, and sensor locations are randomly generated according to a homogeneous PPP for the finite region. The 3D region is large enough to allow for all possible sensor locations that could detect the emitter. We additionally increase the region size further to prevent edge effects when simulating the PPP within the finite region. The emitter and sensor orientations are uniformly random.

Second, we simulate an RF environment governed by (7). Without loss of generality, the simulations do not include fading coefficients (i.e., hj 1). With closed-form gain functions for the real antennas, we can numerically evaluate the gain, g(p, R, t), and calculate p;. We can then evaluate the event E. Using

the Monte Carlo method, we generate many realizations of random deployments and estimate Pr(E) as the fraction of trials in which E occurred.

Across simulated trials, the following conditions hold. The emitter antenna remains the same, but the orientation is always random. The emitter and sensors share the same type of antenna. For instance, if the emitter uses a finite length dipole, the sensors do, as well, though the lengths may be different. Again, if the emitter's antenna is approximated by gain A with the spherical quadrilateral shape, the sensors' antennas are, as well, but with potentially different HPBWs. This design is not necessary to show which approximation is most accurate compared to a real antenna. However, to limit numerous possible combinations, we selected that the sensors and emitter have the same type of antenna to emphasize the effect on Pr(E).

A. Finite Length Dipole

For the finite length dipole, we use the far-field expressions for the normalized radiation intensity given in [29, eq. (4-64)]:

$$U(\theta, \psi) = \left(\frac{\cos\left(\frac{kl}{2}\cos\theta\right) - \cos\left(\frac{kl}{2}\right)}{\sin\theta}\right)^{\frac{2}{2}},$$

where k = 2m/A is the radian spatial frequency, commonly called the wave number, and I is the length of the dipole, commonly given as in terms of the wavelength A such that kl does not depend on A. With [29, Eq. (2-21)], we can determine the gain of the finite length dipole and its HPBW for a given length l. A detailed derivation to find a closed-form expression for the gain is given in [29, Sec. 4.5.4].

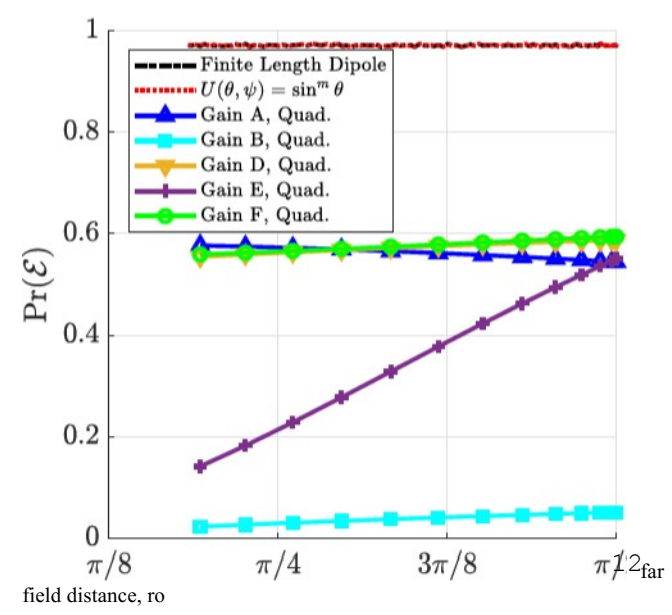
The parameters for the simulation of omnidirectional antennas are in Table II. We vary the length of the dipole for the sensor, which consequently varies the elevation HPBW a^s. The results comparing the finite length dipole to the approximations of the gain function are given in Fig. 9.

We offer a few brief observations. First, if we simulate the gain pattern resulting from (4), the result is indistinguishable from the finite length dipole. This could be useful for future simulations and comparisons because (4) is simpler to analyze and simulate. Second, the gain approximations with results closest to those of the real antenna are gains A and F from Table I. Consequently, our analyses in this work and [12] focus on those particular gain value approximations. We also

TABLE 11 PARAMETERS FOR SIMULATION OF FINITE LENGTH DIPOLE

Parameter	Value
sensor density,	0.016 sensors/m
sensor MDS, TS	-110 dBm
emitter power, pe	-60 dBm
operating frequency, f	1 GHz
emitter elevation HPBW,	0.5743 rad
path loss exponent, a	3





Sensor Half-power Beamwidth, e^s (rad)

Fig. 9. The simulated Pr(E) for a finite length dipole and for the radiation intensity $\sin^m 0$ given in (4). The closed form expressions of Pr(E) for the other approximations in Table I with a spherical quadrilateral shape are provided for comparison.

observe a large gap between the results of the finite length dipole and those of the approximations. The gap indicates the conservative approach in simplifying the gain function. If we were to determine a required sensor density for a given Pr(E), the results indicate that our models produce upper bounds on the sensor density. In particular, let Pr(E) denote the true probability of detection with a real antenna, while Pr(E) denotes the probability of detection given by our model. Since Pr(E) > Pr(E), the sensor density predicted by Pr(E) is much larger than it needs to be to obtain an equivalent value of Pr(E). In other words, the expressions for sensor density in Section III and [12] are upper bounds on the true required sensor density.

B. Patch Antenna

For the microstrip patch antenna, we use the cavity model for a closed form expression of the radiation intensity U (O, V) [29, Sec. 14.2.2]. In particular, a rectangular patch antenna with width W, length L, and height H is modeled as two radiating slots with a dominant TM^{\pounds} mode. The

TABLE 111
PARAMETERS FOR SIMULATION OF DIRECTIONAL PATCH ANTENNA

Value

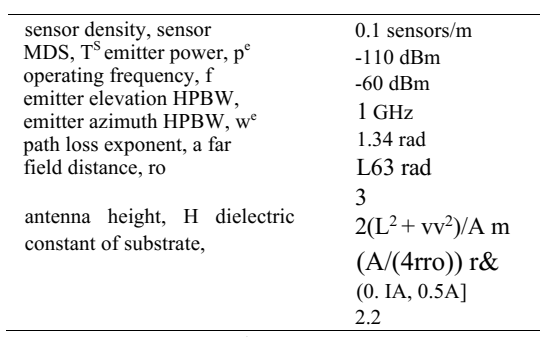


TABLE IV PARAMETERS FOR SIMULATION OF DIRECTIONAL PATCH ANTENNA

Parameter	Value
sensor density, sensor MDS,	0.04 sensors/m
emitter power, pe operating	-110 dBm
frequency, f emitter elevation HPBW, ee emitter azimuth	-60 dBm
HPBW, w e path loss	1 GHz
exponent, a far field distance,	1.77 rad
	1.51 rad
horn waveguide width, a horn	3
waveguide height, b horn flare width	2(L2 + vv2)/A m
and height. al and bl horn altitude length, PI and 22	(A/(4Trro)) r;
length, F1 and 22	0.25A m
	0.25A m
	[0.25A, 0.5Al m
	6A m

normalized radiation pattern is given by

$$= \left[\sin \theta \frac{\sin X}{X} \frac{\sin Z}{Z} \cos \left(\begin{array}{c} \text{kLe} & 2 - \sin \theta \\ \text{O sin} \end{array} \right) \right]$$

$$= \frac{kH}{2} \sin \theta \cos \psi$$

$$Z$$

$$Z = -\cos \phi$$

$$Z = \cos \phi$$

where Le is the effective length of the patch antenna given by [29, eq. (14-3)]. The length and width of the patch antenna are determined via the procedure outlined in [29, Sec. 14.2.1.C] for the substrate RT/duroid 5880, a given height H, and a desired operating frequency of 1 GHz. Again, with [29, eq. (2-21)], we can derive a closed form expression for the gain function.

To simulate the rectangular patch antenna, we use the parameters in Table IV. We vary the sensor's patch antenna height H from 0.1A to 0.5A and find the antenna width W and effective length Le from the procedure in [29, Sec. 14.2.1.C] to achieve efficient antennas that could be used in practice. The changes in antenna geometry result in different antenna patterns and HPBWs. We plot Pr(E) against the resulting HPBWs in Fig. 10. Note that for our patch antenna design, the elevation HPBW and the azimuth HPBW are physically related and cannot be varied independently. Consequently, we show and the corresponding on separate axes. The gain approximations from Table I are based on the same HPBWs as the patch antenna. Note that the symmetric spherical cap shape uses the 1--IPBW to make the approximation conservative because < here. We also simulate the antenna pattern resulting from (3).

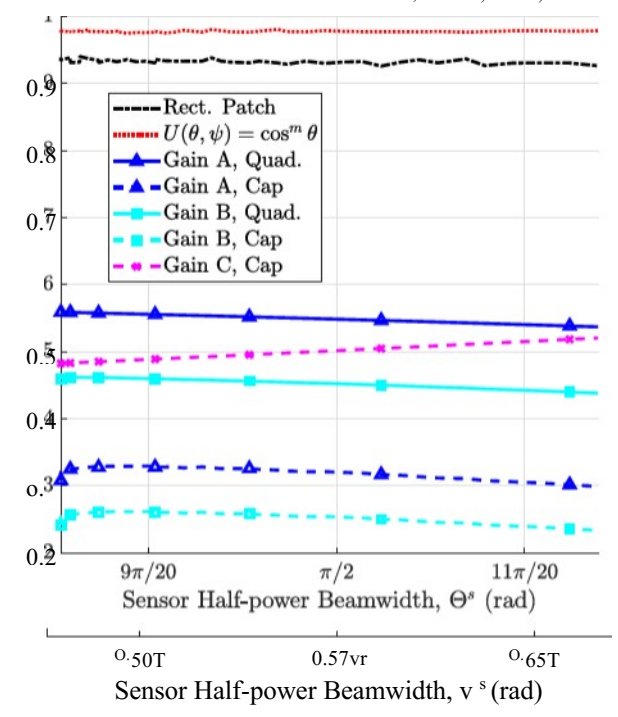


Fig. 10. The simulated Pr(E) for a rectangular patch antenna and for the radiation intensity $\cos^m O$ given in (3). The closed form expressions of Pr(E) for the other approximations of directional antennas in Table I are provided for comparison.

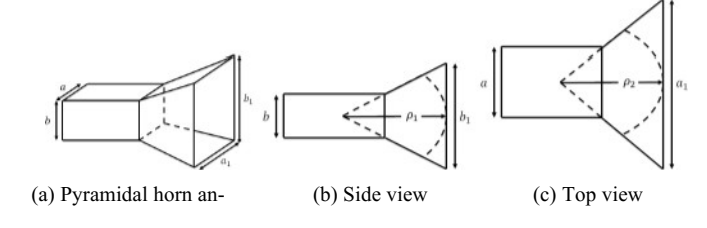


Fig. 11. The geometry of the pyramidal horn antenna, reproduced from [29, Fig. 13.18].

We offer the following observations on the results in Fig. 10. The simulation of (3) overestimates Pr(E) for the patch antenna but is close in value. The closest analytic lower bound is that resulting from the spherical quadrilateral shape with gain A from Table I. Based on the trends of the plotted lines, though, the spherical cap shape with gain C could be a tighter lower bound if larger HPBWs were considered.

C. Horn Antenna

We model the pyramidal horn antenna as outlined in [29, Sec. 13.4]. Fig. 11 shows the geometry of the antenna, matching the notation of [29]. The electric field equations can be found in [29, eq. (13-48)]. After being appropriately scaled and squared [29, eq. (2-12a)], the electric field equations give rise to the normalized radiation intensity U(O, V). For brevity, we omit the full expression and refer the reader to [29, eq. (13-48)], but we note the large complexity of the expression and the frequent occurrence of Fresnel integrals. This indicates that despite

having a closed form expression, the gain of the pyramidal horn antenna is expensive to evaluate.

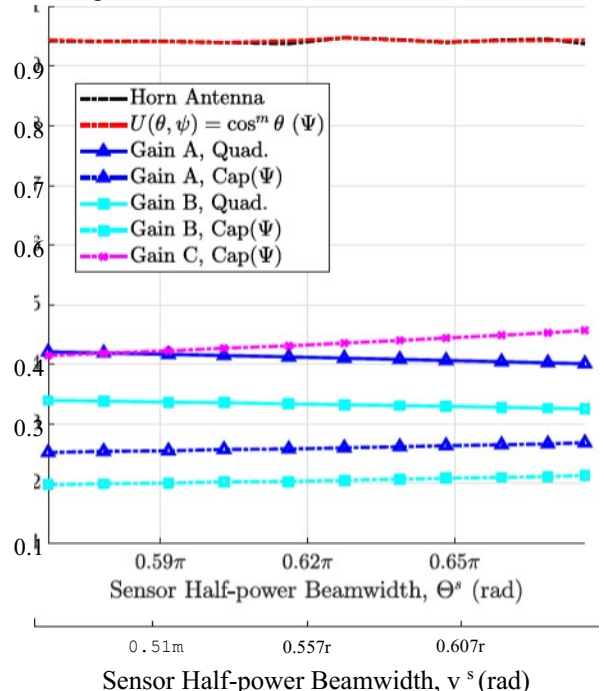


Fig. 12. The simulated Pr(E) for a horn antenna and for the radiation intensity $\cos^m O$ given in (3). The closed form expressions of Pr(E) for the other approximations of directional antennas in Table I are provided for companson.

For the simulation of the directional horn antenna, we use the parameters in Table IV. We vary the sensor's horn antenna flare width UI and height bl simultaneously from 0.25A to 0.5A. Both the waveguide width a and height b are held constant at 0.25A, and PI P2 6A [29, Sec. 13.4]. The changes in the antenna geometry result in different antenna patterns and HPBWs.

We plot Pr(E) against the resulting 1--1PBWs in Fig. 12. Note that for our design of the horn antenna, the elevation HPBW and the azimuth HPBW are physically related and cannot be varied independently. Consequently, we show Θ^s and the corresponding on the bottom axis. The gain approximations from Table I are based on the same HPBWs as the horn antenna. To make the approximation conservative, the symmetric spherical cap shape uses the HPBW because Ψ^s for the horn antenna under consideration. We also simulate (3).

We offer the following observations on the results in Fig. 12. The simulation of (3) closely approximates Pr(E) for the horn antenna. The other approximations significantly underestimate Pr(E). The closest closed-form approximation to the horn antenna result is the spherical cap shape with gain C from Table I. Nonetheless, trend extrapolation indicates that the spherical quadrilateral shape with gain A would be a better approximation for smaller HPBWs.

Ultimately, simulating the horn antenna is time consuming. The simulation of (3) offers a very close approximation with far less computation. For analytic lower bounds, the approximation achieved from the spherical cap shape and gain

C is the tightest of those in this paper.

D. Conclusion

The results from Fig. 9 suggest that when performing our analysis with closed-form expressions for omnidirectional antennas in 3D, we should use the spherical quadrilateral shape with gain F in Table I. Similarly, the results in Fig. 12 suggest that we should use the spherical cap with gain C for directional antennas. Note that gain F and C have inherently assumed shapes of spherical quadrilateral and spherical cap, respectively, so the value and shape models are consistent.

For analysis of closed-form expressions in two dimensions, the shape of both the spherical cap and spherical quadrilateral reduce to the azimuth HPBW W. Since the shape approximations are equivalent in 2D, the accuracy of the gain approximations reduces to the accuracy of go(W, 6). The results in [12] inform us that the optimal antennas will be omnidirectional with narrow elevation beamwidths. Consequently, the results in Fig. 9 suggest the use of gain A for two-dimensional analysis because gain A is more accurate for lower 9 in omnidirectional antennas. Thus, we use gain A for our two-dimensional analysis in [12].

V. FREQUENCY SENSITIVITY AND MULTIPLE FREQUENCY BANDS

A derivation of the frequency sensitivity of Pr(E) is provided in [III, [12] for 2D scenarios. Reproducing the results for 3D is straightforward with the small-angle and Binomial approximations. We briefly discuss the results here for completeness.

For a fixed antenna geometry, the HPBWs and are functions of frequency. Similarly, K is often modeled as having a I/f ² frequency dependence. In practice, we design the sensor antennas for a target frequency, but after deployment, the antennas cannot be modified. Consequently, the performance is sensitive to emitter frequency. With no fading (h I), analysis indicates that Pr(E) in (I I) and in (12) are not affected much if Af/f is small.

Mathematically, let g denote the complement of E. Let us consider a rectangular (or circular) aperture antenna modeled with the Kraus approximation. If we perturb the frequency to f + Af and if IAf/fl 1/4, we obtain

$$(\Pr(\acute{E}) \tag{15}$$

where (4 2ö)Af/f. Both the spherical cap and quadrilateral yield this same result.

For example, if a sensor deployment achieves Pr(E) — .95 for a 3, and we allow no more than a 1 % relative change in Pr(E), then Af/f can range from —0.035 to 0.029. If f is 1 GHz, the frequency can vary —35 MHz to 29 MHz with no more than a 1% change in performance.

Furthermore, the change in performance can be compensated by adjusting the sensor density. In particular, to retain the same performance for a frequency change Af, the new sensor density + should follow

(16)

If Af < 0, then < 0, and if Af > 0, then $\Delta \lambda^{s}$ > 0. In other words, lower frequencies require fewer sensors. This point is helpful in designing a sensor deployment for a frequency range fl to h. In particular, the deployment should be designed for the highest frequency h. For the lower bands, the performance will be better than that of h, or fewer sensors would need to be active to maintain the same performance.

VI. RESULTS FOR MULTIPLE EMITTERS

If we consider multiple emitters, the results are analogous to those in [12, Sec. IV]. Consequently, we briefly write the main results for completeness but refer the reader to [12] for details, derivations, and applications.

Let there be n $^{\rm e}$ arbitrarily located emitters in a finite region R C IR $^{\rm 3}$. Define multi-emitter detection by the sensor network as the event D Ei. We lower bound the probability of multi-emitter detection given n $^{\rm e}$ as

Pr(D I 1 — n e exp
$$\left(-\lambda^s \eta^e \eta^s c_3 \mathbb{E}[h^{\delta}] \omega^{\delta}\right)$$
.

(17) ..., n^e } denote the flumber

Additionally, let n u e {O I of undetected emitters. Given n e , the average number of undetected emitters is

$$\mathbb{E}[\mathbf{n}^{\mathrm{u}}\mathbf{I}\,\mathbf{n}^{\mathrm{e}}]\,\mathbf{n}^{\mathrm{e}}\exp\left(-\lambda^{s}\eta^{e}\eta^{s}c_{3}\mathbb{E}[h^{\delta}]\omega^{\delta}\right). \tag{18}$$

If the emitter locations form an arbitrary stationary point process with density Y, the conditioning in both expressions can be removed by taking the expectation with respect to n^e , where $E[n^e]$, VIRI and IRI denotes the volume of R.

VII. CONCLUSION AND FUTURE WORK

While providing a beneficial baseline for design, the twodimensional SM model in [12] does not provide a satisfying design criterion for elevation HPBW, does not fully represent realistic antenna orientations, and impractically constrains emitter and sensor locations to be co-planar. To address these issues, this paper extends the framework and results to three dimensions. Optimal values of elevation HPBW were presented in Fig. 6 as a function of path loss exponent, a. With optimal HPBWs, we found that certain environments favor different antennas. If a < 3.22, directional antennas are optimal for emitter detection. Otherwise, omnidirectional antennas are optimal. Nonetheless, the performance difference between optimal and suboptimal antennas could be small as shown in Fig. 8. Omnidirectional antennas were found to be a robust choice for environments with varying a. Additionally, the threedimensional model allowed for a survey of various antenna gain models. This paper evaluated these models against simulations of real antenna patterns and verified the models used in this paper and in [12]. Ultimately, this work re-enforced many of the conclusions from [12] while providing additional insight into optimal elevation HPBW and the effects of location and orientation in three dimensions.

Future work should further investigate the use of nonstationary point processes to model more diverse scenarios.

Additionally, the framework could be extended to consider other data products of spectrum monitoring, such as emitter localization and/or transmit power estimation. Further research is needed to determine the system design modifications required to achieve these more complex data products, as well.

APPENDIX A DERIVATION OF OPTIMAL HPBWs

For space considerations, we leave out the complete derivation and present final expressions. For a directional antenna.

$$\begin{split} \frac{\partial}{\partial \Theta} \eta g^{\delta} &= \frac{1}{2} \sin(\Theta/2) \left(\frac{\ln(1/2)}{\ln(\cos\Theta/2)} + 1 \right)^{3/\Theta = \frac{1}{4}} \cdots \\ &\left[\frac{1}{2} \left(\frac{\ln(1/2)}{\ln(\cos\Theta/2)} + 1 \right) + \frac{3}{\alpha} \frac{\ln(1/2)}{\ln^2(\cos\Theta/2)} \frac{\sin^2(\Theta/4)}{\cos(\Theta/2)} \right], \end{split}$$

and for an omnidirectional antenna,

$$\begin{split} \frac{\partial}{\partial \Theta} \eta g^{\delta} &= \frac{1}{2} \left(\frac{\Gamma\left(\frac{\ln(1/2)}{2\ln(\cos\Theta/2)} + \frac{3}{2}\right)}{\sqrt{\pi} \Gamma\left(\frac{\ln(1/2)}{2\ln(\cos\Theta/2)} + 1\right)} \right)^{3/\alpha} \cdots \\ &\left[\frac{3}{2\alpha} \frac{\ln(1/2)}{\ln^2(\cos(\Theta/2))} \frac{\sin^2(\Theta/2)}{\cos(\Theta/2)} \cdots \right. \\ &\left[\varPsi\left(\frac{\ln(1/2)}{2\ln(\cos\Theta/2)} + \frac{3}{2}\right) - \varPsi\left(\frac{\ln(1/2)}{2\ln(\cos\Theta/2)} + 1\right) \right] \cdots \\ &\left. - \text{f- COS(e/2)} \right. \end{split}$$

where the digamma function

$$\underset{\text{IPO}}{\text{IPO}} \triangleq \frac{\mathrm{d}}{\mathrm{d}x} \ln(\Gamma(x)) = \frac{\Gamma'(x)}{\Gamma(x)}.$$

We use a numeric root solver to find the zeros of these derivatives and numerically confirm that the solution is a maximum.

APPENDIX B DERIVATION OF OPTIMAL C AND D

The dotted lines in Fig. 8 have closed-form expressions for any arbitrary C or D, respectively. The expressions can be found by solving $\frac{\partial}{\partial C}|\Pr^*(\mathcal{E})_{dir}-\Pr^*(\mathcal{E})_{omni}|=0$ and $\frac{\partial}{\partial D}|\Pr^*(\mathcal{E})_{dir}-\Pr^*(\mathcal{E})_{omni}|=0$. The results are

$$D^* = \left(\frac{\ln \frac{(\eta_{\text{omni}} g^{\delta}_{\text{omni}})}{(\eta_{\text{dir}} g^{\delta}_{\text{dir}})}}{C\Gamma(1+\delta)\left((\eta_{\text{omni}} g^{\delta}_{\text{omni}}) - (\eta_{\text{dir}} g^{\delta}_{\text{dir}})\right)}\right)^{1/\delta},$$

$$C^* = \frac{\ln \frac{(\eta_{\text{omni}} g^{\delta}_{\text{omni}})}{(\eta_{\text{dir}} g^{\delta}_{\text{dir}})}}{D^{\delta}\Gamma(1+\delta)\left((\eta_{\text{omni}} g^{\delta}_{\text{omni}}) - (\eta_{\text{dir}} g^{\delta}_{\text{dir}})\right)} - (\eta_{\text{dir}} g^{\delta}_{\text{dir}})}.$$

Intuitively, D* and C* indicate parameter values for which the difference in performance between directional and omnidirectional antennas is most significant. As Fig. 8 illustrates, other values of D and C diminish the difference in performance between the two types of antennas.

APPENDIX C DERIVATION OF Pr(E) FOR FCC LATTICE

Let L C 12^3 denote the FCC lattice with a point at the origin, o. Let BV denote the Voronoi cell for point v e L. For the FCC lattice, all Voronoi cells are congruent rhombic dodecahedra. Let denote the randomly shifted FCC lattice, $\Phi = \{v \in L : v + U \}$, where U is uniformly distributed over Bo. Denote as the number of points from in the region W C IR³. Since the all points are translated by U e Bo, we know (b(Bv) 1, Y v e L.

Define Mx, -y, and N as in Prop. 1. Denote $\{x \in \Phi : Mx > Illxll^{\bar{u}}\}$, which has cardinality N. Since the DIX are iid, is an independently thinned version of with probability of retaining a point EM [Il[Mx > = FM(111x110)]•

Given $\mathbf{U}=\mathbf{u}$, Φ is nonrandom ($\Phi=\mathbb{L}+\mathbf{u}$). Thus, $\Pr(\Phi'(\mathcal{B}_{\mathbf{v}})=1\mid \mathbf{U})=\bar{F}_{M}(\gamma\|\mathbf{v}+\mathbf{u}\|^{\alpha})$, and the complement $\Pr(\Phi'(\mathcal{B}_{\mathbf{v}})=0\mid \mathbf{U})=F_{M}(\gamma\|\mathbf{v}+\mathbf{u}\|^{\alpha})$. Therefore,

$$\begin{split} \Pr(N = 0 \mid \mathbf{U}) &= \Pr \bigg(\bigcap_{\mathbf{v} \in \mathbb{L}} \big\{ \Phi'(\mathcal{B}_{\mathbf{v}}) = 0 \big\} \mid \mathbf{U} \bigg) \\ &= \Pr \bigg(\bigcap_{\mathbf{x} \in \mathbb{L} + \mathbf{u}} \big\{ M_{\mathbf{x}} \le \gamma \|\mathbf{x}\|^{\alpha} \big\} \mid \mathbf{U} \bigg) \\ &= \prod_{\mathbf{x} \in \mathbb{L} + \mathbf{u}} F_{M}(\gamma \|\mathbf{x}\|^{\alpha}). \end{split}$$

Given U

The third line results from the iid Mx. Since Pr(E) - — Pr(N > O) I — Pr(N = O), we have

$$Pr(E) = \int_{\mathbb{R}^3} Pr(l | Pr(N > 0 | IU) f_U(u)$$

$$= 1 - \frac{1}{1 - 2 - 2}$$

$$IBOI J B 11 F_M(\gamma ||x||^{\alpha}) du.(19)$$

$$0 \text{ xeII.+u}$$

The region Bo and its volume IBO I are determined by the Iattice spacing a and the rhombic dodecahedron geometry. M and γ are application specific with examples given in Section Ill-B. Unfortunately, (19) does not offer much insight or an easy numeric approach to solve, except perhaps for some closedform expressions of FM. The least cumbersome approach to estimate Pr(E) would likely be simulated Monte Carlo trials for a given a, a, -y, and FM.

ACKNOWLEDGMENT

The authors thank Prof. Martin Haenggi for his thoughtful discussion and feedback on the use of stochastic geometry in this paper.

REFERENCES

- [1] R. Trautmann, "Handbook: Spectrum monitoring," Int. Telecommun. Union (ITU), Geneva, Switzerland, Rep. R-HDB-23, 2011.
- [2] T. T. Nguyen, M. R. Souryal, A. Sahoo, and T. A. Hall, "3.5 GHz environmental sensing capability detection thresholds and deployment," IEEE Trans. cogn. Commun. Netw., vol. 3, no. 3, pp. 437—449, sep. 2017.

- [3] A. Ghosh, R. A. Berry, and V. Aggarwal, "Spectrum measurement markets for tiered spectrum access," IEEE Trans. Cogn. Commun. Netw., vol. 4, no. 4, pp. 929-941, Dec. 2018.
- [4] S. Bhattarai, J.-M. J. Park, B. Gao, K. Bian, and W. Lehr, "An overview of dynamic spectrum sharing: Ongoing initiatives, challenges, and a roadmap for future research," IEEE Trans. Cogn. Commun. Netw., vol. 2, no. 2, pp. 110-128, Jun. 2016.
- [5] M. Palola et al., "Field trial of the 3.5 GHz citizens broadband radio service governed by a spectrum access system (SAS)," in Proc. IEEE Int. Symp. Dyn. Spectr. Access Netw. (DYSPAN), Baltimore, MD, USA, Mar. 2017, pp. 1_9.
- [6] A. Nika, Z Zhang, B. Y. Zhao, and H. Zheng, "Toward practical spectrum permits," IEEE Trans. Cogn. Commun Netw., vol. 3, no. 1, pp. 112-122, Mar. 2017.
- [7] A. Bhattacharya, A. Chakraborty, S. R. Das, H. Gupta, and P. M. Djurié, "Spectrum patrolling with crowdsourced spectrum sensors," IEEE Trans. Cogn. Commun. Netw., vol. 6, no. 1, pp. 271—281, Mar. 2020.
- [8] J. Neel et al., "Big RF for homeland security applications," in Proc. IEEE Int. Symp. Technol. Homeland Security (HST), Waltham, MA, USA, Apr. 2015, pp. 1—6.
- [9] A. Chakraborty, M. S. Rahman, H. Gupta, and S. R. Das, "SpecSense: Crowdsensing for efficient querying of spectrum occupancy," in Proc. IEEE conf. Comput. Commun. (INFOCOM), Atlanta, GA, USA, 2017, pp. 1—9.
- [10] X. Liu, Q. Sun, W. Lu, C. Wu, and H. Ding, "Big-data-based intelligent spectrum sensing for heterogeneous spectrum communications in 5G," IEEE Trans. Wireless Commun., vol. 27, no. 5, pp. 67—73, Oct. 2020.
- [1 1] N. G. Kleber, "The design of widespread spectrum monitoring systems," Ph.D. dissertation, Dept. Elect. Eng., Univ. Notre Dame, Notre Dame, IN, USA, 2021.
- [121 N. Kleber, M. Haenggi, J. Chisum, B. Hochwald, and J. N. Laneman, "Directivity in RF sensor networks for widespread spectrum monitoring," IEEE Trans. Cogn. Commun. Netw., early access, Nov. 13, 2021, doi: 10.1 109, rccN.2021.3124523.
- [131 B. Shah and K.-I. Kim, "A survey on three-dimensional wireless ad hoc and sensor networks," Int. J. Distrib Sens. Netw., vol. 10, no. 7, pp. 1-20, 2014.
- [141 G. Eappen, T. Shankar, and R. Nilavalan, "Advanced squirrel algorithmtrained neural network for efficient spectrum sensing in cognitive radio-based air traffic control application," IET Commun., vol. 15, no. 3, pp. 1326-1351, 2021.
- [15] M. Zafer, M. R. Senouci, and M. Aissani, "0n coverage of 3D terrains by wireless sensor netu'orks," in Proc. Federated Conf Comput. Sci. Inf. syst. (FedCSIS), Leipzig, Germany, 2019, pp. 501-504.
- [16] B. Cao, J. Zhao, Z Lv, and X. Liu, "3D terrain multiobjective deployment optimization of heterogeneous directional sensor networks in security monitoring," IEEE Trans. Big Data, vol. 5, no. 4, pp. 495—505, Dec. 2019.
- [17] B. cao, J. Zhao, p Yang, p. Yang, X. Liu, and Y. Zhang, "3-1) deployment optimization for heterogeneous wireless directional sensor networks on smatt city," IEEE Trans. Ind. Informat., vol. 15, no. 3, pp. 1798-1808, Mar. 2019.
- [18] A. Saad, M. R. Senouci, and O. Benyattou, "Toward a realistic approach for the deployment of 3D wireless sensor networks," IEEE Trans. Mobile Comput., early access, sep. 18, 2020, doi: 10.1109/TMC.2020.3024939.
- [19] K. Zaimen, M.-E.-A. Brahmia, J.-F. Dollinger, L. Moalic, A. Abouaissa, and L. Idoumghar, "A overview on WSN deployment and a novel conceptual BIM-based approach in smart buildings," in Proc. 7th Int. Conf. Internet Things Syst. Manage. Security (IOTSMS), Paris, France, 2020.
- [20] N. Kleber et al., **Radiohound: A pervasive sensing platform for sub6 GHz dynamic spectrum monitoring," in Proc. IEEE Int. Symp. Dyn. spectr. Access Netw (DYSPAN), Baltimore, MD, USA, Mar. 2017, pp. 1—2
- [21] L. Zhang, T.-T. Liu, F.-Q. wen, L. Hu, C. Hei, and K. Wang, "Differential evolution based regional coverage-enhancing algorithm for directional 3D wireless sensor networks," IEEE Access, vol. 7, pp. 93690-93700, 2019.
- [22] H. Jung and I.-H. Lee, "Analog cooperative beamforming with spherically-bound random arrays for physical-layer secure communications," IEEE Commun. Lett., vol. 22, no. 3, pp. 546-549, Mar.

- [23] H. Jung and I.-H. Lee, "Secrecy performance analysis of analog cooperative beamforming in three-dimensional Gaussian distributed wireless sensor networks," IEEE Trans. Wireless Commun., vol. 18, no. 3, pp. 1860-1873, Mar. 2019.
- [24] L. Zhang, Z Wang, Z Kuang, and H. Yang, "Three-dimensional læalization algorithm for WSN nodes based on RSSI-TOA and LSSVR method," in Proc. 11th Int. Conf. Meas. Technol. Mechatronics Autom. (ICMTMA), Qiqihar, China, 2019, pp. 498-503.
- [25] P. Zuo et al., "Directional source localization based on RSS-AOA combined measurements," China Commun., vol. 17, no. 11, pp. 181— 193, Nov. 2020.
- [26] Z Wei, J. Zhu, Z. Guo, and F. Ning, "The performance analysis of spectrum sharing between UAV enabled wireless mesh networks and ground networks," IEEE Sensors 1, vol. 21, no. 5, pp. 7034-7045, Mar. 2021. [27] M. Haenggi, Stochastic Geometry for Wireless Networks. New York, NY, USA: Cambridge Univ. Press, 2013.
- [28] D. M. Pozar, Microwave Engineering, 4th ed. Hoboken, NJ, USA: Wiley, 2012.
- [29] C. A. Balanis, Antenna Theory': Analysis and Design, 3rd ed. Hoboken, NJ, USA: Wiley, 2005.
- [30] M. F. Iskander, Electromagnetic Fields and Waves. Englewood Cliffs, NJ, USA: Waveland Press, 1992.
- [31] J. D. Kraus, Antennas, 2nd ed. New York, NY, USA: McGraw-Hill Book Company, 1988.
- [32] C.-T. Tai and C. Pereira, "An approximate formula for calculating the directivity of an antenna," IEEE Trans. Antennas Propag., vol. 24, no. 2, pp. 235-236, Mar. 1976.
- [33] N. McDonald, "Approximate relationship between directivity and beamwidth for broadside collinear arrays," IEEE Trans. Antennas Propag., vol. 26, no. 2, pp. 340-341, Mar. 1978.
- [34] D. Pozar, "Directivity of omnidirectional antennas," IEEE Antennas Propag. Mag., vol. 35, no. 5, pp. 50—51, Oct. 1993.
- [35] A. Goldsmith, Wireless Communications. New York, NY, USA: Cambridge Univ. Press, 2005.
- [36] V. Erceg et al., "An empirically based path loss model for wireless channels in suburban environments," IEEE J. Sel. Areas Commun., vol. 17, no. 7, pp. 1205-1211, Jul. 1999.
- [37] J. Møller and E P Schoenberg, "Thinning spatial point processes into Poisson processes," Adv. Appl. Probab., vol. 42, no. 2, pp. 347—358, 2010
- [381 T. C. Hales, "A proof of the Kepler conjecture," Ann. Math., vol. 162, no. 3, pp. 1065-1185, 2005.
- [391 X. Tang, X. Xu, and M. Haenggi, "Meta distribution of the SIR in moving networks," IEEE Trans. Commun, vol. 68, no. 6, pp. 3614-3626, Jun. 2020.



Nikolaus Kleber (Member, IEEE) received the B.S., M.S., and Ph.D. degrees in electrical engineering from the University of Notre Dame, Notre Dame, IN, USA, in 2013, 2016, and 2021, respectively.

He joined Raytheon Technologies in 2019 and is currently a Senior Software Engineer. His research interests include signal processing, interferencelimited communications, and distributed spectrum monitoring.



Jonathan D. Chisum (Senior Member, IEEE) received the Ph.D. degree in electrical engineering from the University of Colorado at Boulder, Boulder, CO, USA, in 2011.

From 2012 to 2015, he was a Member of Technical Staff with the Massachusetts Institute of Technology Lincoln Laboratory in the Wideband Communications and Spectrum Operations groups. His work with Lincoln Laboratory focused on millimeter-wave phased arrays, antennas, and

transceiver design for electronic warfare applications. In 2015, he joined as a Faculty of the University of Notre Dame, where he is currently an Assistant Professor of Electrical Engineering. His group focuses on gradient index (GRIN) lenses for low-power millimeter-wave beam-steering antennas, nonlinear (I-bit) radio architectures for highly efficient communications and sensing up through millimeter-waves, phase-change materials for reconfigurable RF circuits for wideband distributed circuits and antennas, and microwave/spin-wave structures for low-power and chip-scale analog signal processing for spectrum sensing and protection. His research interests include millimeter-wave communications and spectrum sensing using novel and engineered materials and devices to dramatically lower the power and cost and enable pervasive deployments.

Dr. Chisum is a member of the American Physical Society, and an elected Member of the U.S. National Committee (USNC) of the International Union or Radio Science's (URSI) Commission D (electronics and photonics). He is the past Secretary and the current Vice-Chair for USNC URSI Commission D: Electronics and Photonics.



Bertr New degre USA, Duke degre engin USA. Fro Bertrand Hochwald (Fellow, IEEE) was born in New York, NY, USA. He received the bachelor's degree from Swarthmore College, Swarthmore, PA, USA, the M.S. degree in electrical engineering from Duke University, Durham, NC, USA, and the M.A. degree in statistics and the Ph.D. degree in electrical engineering from Yale University, New Haven, CT,

From 1986 to

1989, he was with the Department of Defense, Fort Meade, MD, USA. He was a Research Associate and a Visiting Assistant Professor with the Coordinated Science Laboratory, University of Illinois at Urbana—Champaign, Urbana, IL USA. In 1996, he joined the Mathematics of Communications Research Department, Bell Laboratories, Lucent Technologies, Murray Hill, NJ, USA, where he was a Distinguished Member of the Technical Staff. In 2005, he joined Beceem Communications, Santa Clara, CA, USA, as the Chief Scientist and the Vice-President of Systems Engineering. He served as a Consulting Professor of Electrical Engineering with Stanford University, Palo Alto, CA, USA. In 2011, he joined the University of Notre Dame, Notre Dame, IN, USA, as a Freimann Professor of Electrical Engineering. Since 2018, he has been the Co-Director of the Wireless Institute. He has 47 patents and has co-invented several well-known multiple-antenna techniques, including a differential method, linear dispersion codes, and multiuser vector perturbation methods.

Dr. Hochwald received several achievement awards while employed at the Department of Defense and the Prize Teaching Fellowship at Yale University. He received the 2006 Stephen O. Rice Prize for the best paper published in the IEEE TRANSACTIONS ON COMMUNICATIONS. He coauthored a paper that won the 2016 Best Paper Award by a young author in the IEEE TRANSACTIONS ON CIRCUITS AND SYSTEMS. He also won the 2018 H. A. Wheeler Prize Paper Award from the IEEE TRANSACTIONS ON ANTENNAS

AND PROPAGATION. His Ph.D. students have won various honors for their Ph.D. research, including the 2018 Paul Baran Young Scholar Award from the Marconi Society. He is listed as a Thomson Reuters A-lost Influential Scientific Mind in multiple years. He has served as an editor of several IEEE journals and has given plenary and invited talks on various aspects of signal processing and communications. He was elected a Fellow of the National Academy of Inventors in 2019.



J. Nicholas Laneman (Fellow, IEEE) received the Ph.D. degree in electrical engineering and computer science from the Massachusetts Institute of Technology. He is the Director of SpectrumX with the NSF Spectrum Innovation Center, a Founding Director and currently the Co-Director of the Wireless Institute, College of Engineering, and a Professor with the Department of Electrical Engineering, University of Notre Dame. He has authored or coauthored on over 145 publications and

is co-inventor on eight U.S. patents. His research and teaching interests are in wireless system design, radio spectrum access, technology standards and intellectual property, and regulatory policy. He has received the IEEE Kiyo Tomiyasu Award, the Presidential Early-Career Award for Scientists and Engineers, and the NSF CAREER Award, and has been recognized twice by Thomson Reuters as an ISI Highly Cited Researcher.